

Structural Parameters, NLO, HOMO, LUMO, MEP, Chemical Reactivity Descriptors, Mulliken-NPA, Thermodynamic Functions, Hirshfeld Surface Analysis and Molecular Docking of 1,3-Bis(4-methylphenyl)triazine

Hilal Nur Yoğurtçu^a, Cem Cüneyt Ersanlı^{b,1}

^a Sinop University, Institute of Graduate Studies, Department of Physics, Sinop, Türkiye
ORCID ID: 0009-0009-9762-5595

^b Sinop University, Faculty of Arts and Science, Department of Physics, Sinop, Türkiye
ORCID ID: 0000-0002-8113-5091

Abstract

In the current study, the molecular geometry, electronic characteristics, nonlinear optical (NLO) properties, and potential biological activity of 1,3-bis(4-methylphenyl)triazene (**I**) were investigated by a combination of experimental crystallographic data and density functional theory (DFT) calculations at the B3LYP/6-311++G(d,p) level. The optimized molecular geometry was in very good agreement with experimental X-ray data, with a low root-mean-square deviation (RMSD) of 0.106 Å, verifying the computational model. The molecule demonstrated high NLO activity, possessing a first-order hyperpolarizability roughly seven times larger than that of urea, and potential application in optoelectronic and photonic devices. Frontier molecular orbital (FMO) calculation demonstrated HOMO–LUMO energy gap of 5.6015 eV in the gas-phase indicating kinetic stability, and solvent-phase calculation indicated higher reactivity and polarity at high-dielectric conditions. Global reactivity descriptors and molecular electrostatic potential (MEP) mapping identified key electrophilic and nucleophilic sites, with implications for the charge distribution of the molecule and probable modes of interaction. Mulliken and natural population analyses (NPA) also revealed electronic behavior, NPA providing more chemically meaningful charge partitioning. Thermodynamic properties -entropy, enthalpy, and heat capacity- exhibited smooth temperature dependence, which established the thermal stability of the compound. Hirshfeld surface and 2D fingerprint plots of the crystal structure highlighted the dominant role played by van der Waals interactions in crystal packing. Molecular docking studies with the HER2 receptor (PDB ID: 3PP0) showed good binding affinity (-9.8 k cal mol⁻¹) with the aid of supporting hydrogen bonding and hydrophobic interactions with prominent amino acid residues, which reflected potential anticancer activity. Combined, the findings emphasize the exciting multifunctionality of **I**, whose potential uses range from materials science to being a lead scaffold in drug design, particularly for HER2-targeted anticancer drugs.

Keywords: “Quantum mechanical calculations, Hirshfeld surface analysis, molecular docking.”

1. Introduction

Triazene derivatives are characterized by a diazoamino (–N=N–N–) linking two aryl or alkyl groups [1]. Triazenes have this property in that they become isoelectronic with azobenzenes and produce reactive diazonium intermediates in situ, the foundation of their chemical and biological diversity. In fact, there are numerous triazene compounds and they have various applications: they are employed as chemical reagents and synthons in synthesis [1] and they exhibit a variety of bioactivity. For example, several triazenes have been investigated for antimicrobial, anti-inflammatory, antioxidant and anticancer activity [1]. Clinically, the alkylating chemotherapeutic agents dacarbazine and temozolomide are triazene derivatives that methylate DNA to yield antitumor activity [2]. New diaryltriazene analogues (*e.g.*, 1,3-diaryltriazene compounds) have more recently been synthesized and reported to possess strong biological effects – *e.g.*, Figueirêdo et al. (2021) reported new 1,3-diaryltriazene derivatives with promising antimicrobial and anticancer activities [1]. These findings demonstrate the pharmacological value of the triazene framework and impel investigation of similar compounds. A biologically highly relevant target in oncology is the human epidermal growth factor receptor 2 (HER2, also known as ErbB2). HER2 is a transmembrane receptor tyrosine kinase protein participating in cell survival and proliferation, the gene amplification or protein overexpression being responsible for oncogenic signaling in multiple tumors [3]. In breast cancer, 15-30% of tumors are HER2-positive, indicative of aggressive disease but rendering the patient eligible for HER2-targeted therapy [3,4]. Indeed, the generation of HER2 inhibitors (such as the monoclonal antibody trastuzumab and the kinase inhibitor lapatinib) has substantially transformed the outcome in HER2-positive malignancies [4]. As HER2-positive tumors remain an important clinical challenge, the discovery of new small-molecule HER2

¹ Corresponding Author
E-mail Address: ccersanli@sinop.edu.tr

antagonists continues to be a research focus. Here, **I** – a diaryltriazene – is of interest as a lead; its planarity and electron-rich diazoamino linkage could facilitate interaction with kinase domains, but its HER2-binding properties have not been investigated. To investigate such possibilities, we employ computational chemistry methods. Density functional theory (DFT) provides accurate quantum-mechanical data on the optimized geometry of a molecule, frontier orbital energies, charge distribution, and related electronic properties [5]. Ouma et al. (2024) note that DFT achieves a reasonable balance between accuracy and efficiency for the exploration of small drug-like molecule [5], for example, DFT is able to reliably estimate bond strengths, ionization potentials, and relative conformational energies that determine reactivity [5]. Concurrently, molecular docking simulations mimic how a ligand will bind into a protein's active site and determine its binding affinity. Docking is commonly utilized in structure-based drug discovery owing to its ability to screen candidates rapidly and anticipate critical interactions with a target [6]. As an example, Lamichhane et al. (2023) applied docking and molecular dynamics to discover phytochemical HER2 inhibitors [4], demonstrating the capability of in silico screening to rank emerging anticancer agents as high priority. In summary, the combination of DFT and docking allows one to define the intrinsic electronic structure of a compound and predict its ability to interact with a biologically relevant target, thus guiding subsequent experimental investigation. This strategy is validated by previous research on diaryltriazene compounds. As discussed previously, Figueirêdo et al. (2021) synthesized and characterized some 1,3-diaryltriazene derivatives and reported extensive antimicrobial and antitumor activities [1]. These experimental results suggest that diaryltriazenes can interact with a range of biological targets, but the molecular mechanism of action is not known. To our knowledge, no other study has examined **I** by quantum chemistry or protein-binding modeling. This study, we perform DFT calculation for this compound to yield its optimized structure and electronic descriptors (*e.g.*, HOMO–LUMO gap, electrostatic potential) and then proceed with docking simulation against HER2 kinase domain. This theoretical exploration is aimed toward insight into the reactivity profile of the compound and possible mode of binding with HER2 and providing hypothesis regarding its pharmaceutical application.

2. Materials and Method

All quantum chemical calculations in this study were performed with the assistance of the Gaussian 03 program package [7]. The molecular geometries were optimized by minimizing the overall energy with respect to all the geometrical parameters without applying any symmetry constraints. DFT calculations were performed using the B3LYP exchange-correlation functional [8,9] and the 6-311++G(d,p) basis set, implemented in a computational framework similar to that of the Gaussian 03 software. GaussView program [10] was used to visualize the optimized molecular structure. To estimate NLO properties, total molecular dipole moment (μ), mean polarizability (α), and first-order hyperpolarizability (β) were calculated at the same level of theory. Since the output values of α and β from Gaussian are atomic units (a.u.), they were converted to electrostatic units (e.s.u.) using the following conversion factors: α (1 a.u.) = 0.1482×10^{-24} e.s.u. and β (1 a.u.) = 8.6393×10^{-33} e.s.u.

The following equations were used to compute the overall values:

Total Molecular Dipole moment:

$$\mu_{\text{total}} = (\mu_x^2 + \mu_y^2 + \mu_z^2)^{1/2} \quad (1)$$

Average polarizability:

$$\alpha = \frac{1}{3}(\alpha_{xx} + \alpha_{yy} + \alpha_{zz}) \quad (2)$$

$$\beta_{\text{total}} = (\beta_x^2 + \beta_y^2 + \beta_z^2)^{1/2} \quad (3)$$

Total first-order hyperpolarizability:

Where

$$\begin{aligned} \beta_x &= \beta_{xxx} + \beta_{xyy} + \beta_{xzz} \\ \beta_y &= \beta_{yyy} + \beta_{xxy} + \beta_{yzz} \\ \beta_z &= \beta_{zzz} + \beta_{xxz} + \beta_{yyz} \end{aligned} \quad (4)$$

HOMO-LUMO energy levels were calculated in order to analyze the electronic structure and reactivity of the compound. The MEP surface was calculated by the B3LYP/6-311++G(d,p) method in order to identify the possible reactive zones and intra- and intermolecular interactions. The electron acceptor is LUMO, whose energy equals the electron affinity ($EA = -E_{LUMO}$), while the

electron donor is HOMO, and the ionization potential is $IP = -E_{HOMO}$. Based on these, Parr et al. (1999) proposed the global electrophilicity index (w), a measure of the electron-accepting capacity of a molecule and calculated by [11]:

$$w = \frac{\mu^2}{2\eta} \quad (5)$$

Here, η is the overall hardness and μ the chemical potential, defined as:

$$\eta = \frac{E_{LUMO} - E_{HOMO}}{2} = \frac{IP - EA}{2} \quad (6)$$

$$\mu = \frac{E_{LUMO} + E_{HOMO}}{2} = \frac{-(EA + IP)}{2} \quad (7)$$

Other global reactivity descriptors were calculated, including:

Global softness:

$$S = \frac{1}{2\eta} \quad (8)$$

Absolute electronegativity:

$$\chi = -\mu = \frac{IP - EA}{2} \quad (9)$$

Maximum number of electrons that a system can hold:

$$\Delta N_{max} = \frac{(IP + EA)}{2(IP - EA)} = -\frac{\mu}{2\eta} \quad (10)$$

All the descriptors were computed at the B3LYP/6-311++G(d,p) level of theory. The computations were performed in the gas-phase and in six solvents [benzene, dichloromethane, ethanol, methanol, dimethyl sulfoxide (DMSO), and Water] using the Polarizable Continuum Model (PCM) [12]. Thermodynamic properties such as heat capacity, entropy, and enthalpy were computed at temperatures ranging from 100 K to 1000 K. Additional analyses like Mulliken atomic charges, and NPA were performed with the same DFT method. Hirshfeld surface [13,14], and 2D fingerprint [15] plots were obtained using CrystalExplorer Version 17.5 software from the input crystallographic information file (CIF) [13]. Hirshfeld surface analysis [15,16] was performed to study the visualization of intermolecular interactions and identify the hydrophilic nature of the compound. Normalized contact distance (d_{norm}) is definable and estimable by using the equation:

$$d_{norm} = \frac{d_i - r_i^{vdw}}{r_i^{vdw}} + \frac{d_e - r_e^{vdw}}{r_e^{vdw}} \quad (11)$$

In the above equation, d_e and d_i are the distance from the nearest atom outside and inside of the surface, respectively, and both of these distances are utilized to define the normalized contact distance (d_{norm}). The values of d_{norm} are illustrated on the Hirshfeld surface by a red-blue-white (RBW) color scheme. Finally, molecular docking experiments were performed to investigate the interaction between the target compound and the HER2 mutant protein receptor (PDB ID: 3PP0) [17]. Docking simulations were performed using AutoDock 1.5.6 [18], and the data were visualized using Biovia Discovery Studio [19].

3. Results and discussion

3.1. Optimized Geometry

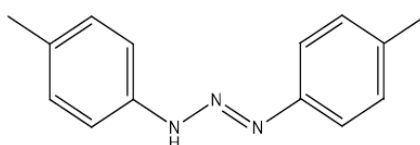


Fig. 1. Chemical diagram of I.

Since the single-crystal X-ray structure of compound **I** was previously reported [20], the present study used those crystallographic data without redetermination. The molecular structure, shown in Fig. 1, was obtained through the experimental techniques described in the cited work. Monoclinic, space group $P2_1/n$ crystallographic data of compound **I** have been found with cell dimensions $a = 14.4024$ (19), $b = 4.8171$ (4), $c = 17.840$ (2) Å and $V = 1237.3$ (3) Å³. Fig. 2(a) gives an ORTEP-III view of the molecular structure of compound **I**. Optimized parameters (bond angles, bond lengths, and dihedral angles) of the title compound were derived [see Fig. 2(b)]. The overlap of the X-ray crystal structure (red) and the density functional theory (DFT)-optimized geometry (blue) of **I**, with a root-mean-square deviation (RMSD) of only 0.106 Å, indicates a very high level of agreement between theoretical and experimental molecular structures [see Fig. 2(c)]. This very low RMSD indicates that the DFT technique correctly captures the structural features displayed in the solid state, thereby supporting the validity of the employed computational model [9,22]. The very good superimposition throughout the entire molecule implies a modest level of conformational flexibility, likely caused by the rigidity imposed by the aromatic and triazene units, which strengthens the molecule's stability further in isolated and crystalline media. This strong convergence validates the efficiency of DFT, particularly hybrid functionals like B3LYP, in accurately describing the geometry of equivalent aromatic triazenes [22].

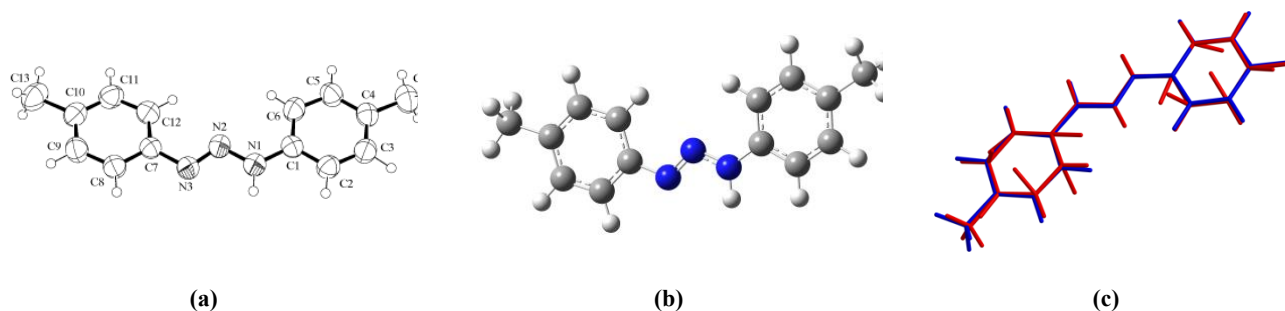


Fig. 2. (a) Reproduced experimental molecular structure of the title compound taken from ref [20], 2005. Displacement ellipsoids are represented at the 50% probability level. (b) Theoretically optimized geometric structure of the title compound. (c) Overlap of the X-ray structure (red) of the title compound and its DFT optimized counterpart (blue) (RMSD 0.106).

The experimental and calculated bond distances and bond angles are compared in Table 1. The gas-phase comparison between experimental (X-ray) and theoretical (DFT-B3LYP/6-311++G(d,p) set) bond lengths and angles reveals some interesting aspects. The theoretical bond lengths are very similar to the experimental ones, with small differences typically ranging from 0.0003 Å to 0.02 Å, which shows that the gas-phase DFT model accurately represents the molecular structure [9]. For example, the N1-N2 bond length is practically identical for both theoretical and experimental measures (1.332 Å and 1.3317 Å), with good agreement between the two methods. However, there are minor differences in certain bonds, i.e., the N2-N3 bond, where the theoretical [1.2580 Å] is shorter than the experimental [1.278(2) Å] value. This difference could be a result of the idealized nature of the gas-phase model, which doesn't include intermolecular forces and solvent effects that can influence the bond length in a real system. Similarly, the calculated bond angles also show good agreement with experimental data, the deviations being largely within 1°, as usual in gas-phase DFT calculations [21]. For instance, the N2-N1-C1 bond angle is 120.35(17)° experimentally and 120.922° calculated, differing by a mere 0.57°, reflecting minor overestimation of the angle in the gas-phase. The gas-phase model would also anticipate bond angles to be somewhat larger in some cases, such as the N1-N2-N3 angle [112.07(15)° experimental vs. 112.776° theoretical], owing to the lack of steric interactions or packing effects that occur in a condensed phase [23]. Overall, gas-phase DFT calculations exhibit excellent agreement with experimental values for both bond angles and bond lengths, with small deviations expected from the neglect of environmental contributions in the computational model. These results suggest the DFT-B3LYP/6311++G(d,p) method as a reliable method for the prediction of molecular geometries, even in the isolated gas-phase, and small discrepancies as the consequence of intrinsic limitations in the method.

Table 1. Ground state geometries of title compound: experimental and optimized. Bond lengths (Å) and angles (°) with e.s.d.s in parentheses.

Bond Distances, Bond and Torsion Angles	Experimental [20]	Theoretical
N1-N2	1.332(2)	1.3317
N1-C1	1.393(2)	1.3986
N2-N3	1.278(2)	1.2580
N3-C7	1.430(2)	1.4336
C1-C2	1.375(2)	1.3819
C1-C6	1.390(2)	1.3998
C4-C14	1.507(2)	1.5095
C7-C8	1.366(2)	1.3774
C7-C12	1.381(2)	1.3848
C10-C13	1.516(2)	1.5089
N2-N1-C1	120.35(17)	120.922

Table 1. Ground state geometries of title compound: experimental and optimized. Bond lengths (Å) and angles (°) with e.s.d.s in parentheses. (Continued)

Bond Distances, Bond and Torsion Angles	Experimental [20]	Theoretical
N1-N2-N3	112.07(15)	112.776
N2-N3-C7	112.65(14)	113.295
N1-C1-C2	118.56(17)	118.501
N1-C1-C6	122.71(18)	122.302
N3-C7-C8	115.97(17)	115.823
N3-C7-C12	125.41(18)	125.285
C8-C7-C12	118.61(19)	118.892
C9-C10-C13	120.49(19)	121.534
C11-C10-C13	121.8(2)	120.654
C1-N1-N2-N3	177.21(15)	179.888
N1-N2-N3-C7	177.97(14)	179.963
N1-C1-C2-C3	177.64(18)	177.874
N3-C7-C8-C9	179.17(17)	179.990
N3-C7-C12-C11	-179.82(18)	-179.984

3.2. NLO Properties

The NLO nature of **I**, predicted at the DFT-B3LYP/6-311++G(d,p) theoretical level, demonstrates that the compound has high prospects for photonic and optoelectronic technology (Table 2). The total dipole moment (μ_{total}) is predicted to be 0.8640 D, representing moderate polarity, which could be beneficial to favor intramolecular charge transfer (ICT) a key factor for second-order NLO materials [21]. The mean polarizability (α) is 29.29036 Å³ from the principal components $\alpha_{xx} = 403.9525$ a.u., $\alpha_{yy} = 188.9018$ a.u., and $\alpha_{zz} = 105.8427$ a.u., which means that the molecule should be highly polarizable, particularly along the x-axis. Most importantly, the first hyperpolarizability (β_{total}) is calculated to be 9.4976×10^{-30} e.s.u., approximately 7.29 times the reference value of urea (1.30×10^{-30} e.s.u. at the same theory level) [24]. The enhancement reflects strong second-order NLO activity, with the enormous β_{xxx} contribution (1158.3794 a.u.) being primarily responsible for dominating the molecular response along the x-axis. The large β units reflect efficient ICT across the conjugated structure due to the electron-donating methyl groups and electron-accepting triazene ring. These features make the compound of special interest for materials applications in areas like frequency doubling, electro-optic modulation, and optical switching.

Table 2. Calculated dipole moments (μ), polarizability (α) and first hyperpolarizability (β) components for **I.**

μ_x	-0.3257 a.u.	β_{xxx}	1158.3794 a.u.
μ_y	0.0968 a.u.	β_{xxy}	-9.3958 a.u.
μ_z	0.0119 a.u.	β_{xyy}	-53.1846 a.u.
μ_{total}	0.8640 D	β_{yyy}	-116.4266 a.u.
α_{xx}	403.9525 a.u.	β_{xxz}	18.8178 a.u.
α_{xy}	0.8290 a.u.	β_{xyz}	-11.4859 a.u.
α_{yy}	188.9018 a.u.	β_{yyz}	5.4292 a.u.
α_{xz}	-0.6433 a.u.	β_{xzz}	-11.3057 a.u.
α_{yz}	0.1339 a.u.	β_{yzz}	16.7442 a.u.
α_{zz}	105.8427 a.u.	β_{zzz}	7.9086 a.u.
α	29.29036 Å ³	β_{total}	9.4976×10^{-30} e.s.u.

3.3. HOMO, LUMO and MEP

The spatial distributions of **I**'s highest occupied molecular orbital (HOMO) and lowest unoccupied molecular orbital (LUMO) were calculated using DFT with the B3LYP functional and 6-311++G(d,p) basis set [8]. As indicated from Fig. 3(a), HOMO tends to be generally delocalized across the triazene moiety (-N=N-NH-) and into the conjugated π -skeleton of the phenyl rings adjacent, particularly the para positions of methyl-substituted phenyl groups. Delocalization of such electron density in the HOMO means very strong π -conjugation and thus raises the electron-donating nature of the molecule. This localization indicates that these regions are very likely to be involved in oxidation reactions or electrophilic interactions [11]. In contrast, the LUMO is highly localized on one phenyl ring and has minimal overlap with the triazene functionality. The electron-deficient character of the LUMO indicates that the region of the molecule is more reactive to nucleophilic attack and can act as an electron acceptor. The spatial distancing of HOMO and LUMO zones from what is observed indicates successful charge transfer when excited, a desirable property in optoelectronic materials and NLO devices. Secondly, the fairly good energy gap between the HOMO and LUMO is indicative of balance in between molecular stability and chemical reactivity, which is vital in molecule design with controllable electronic properties [11, 25].

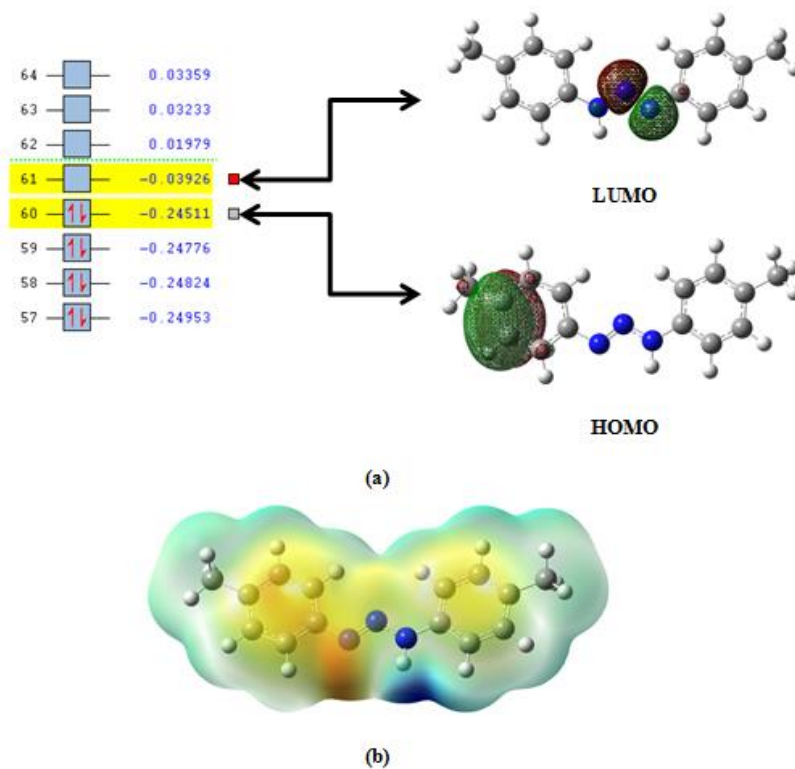


Fig. 3. The HOMO and LUMO distributions (a) and MEP map (b) of **I**.

The molecular electrostatic potential (MEP) surface, which is plotted in the energy range of -0.03998 to $+0.03998$ atomic units (a.u.), gives a three-dimensional representation of the electrostatic charge distribution on the molecular surface [Fig. 3(b)]. It is employed to predict electrophilic and nucleophilic attack sites based on local electron density. For **me**, the most negative possible region (-0.02827 a.u.) is the area around the nitrogen atom N3 of the triazene group. This very electronegative region suggests high electrophilic attack susceptibility by localized lone pairs and resonance stabilization. The most positive region of the electrostatic potential appears in the area around the hydrogen atom H1N with an approximate value of $+0.03935$ a.u. This position is analogous to the hydrogen on the terminal $-NH-$ group of the triazene unit. Its high positive potential suggests its propensity for nucleophilic interaction, which can involve the formation of hydrogen bonds in intermolecular or biological environments. The electrostatic potential smooth gradient across the aromatic rings and triazene bridge is characteristic of a polar molecular surface, which plays a significant role in determining the compound's interaction with polar solvents and biological macromolecules [26]. This congruence of MEP values indicates that the molecule possesses well-defined regions of electrophilic and nucleophilic character, which not only overlap with frontier orbital distribution but also contribute to the transparency of the molecule's character in chemical and biological systems. This is particularly important for applications such as drug design and molecular docking, where local charge differences influence binding affinity and specificity [27].

3.4. Global Reactivity Descriptors

Frontier molecular orbital energies and global reactivity parameters of **I** were computed in the gas-phase and in six solvents, *viz.* benzene, dichloromethane, ethanol, methanol, DMSO, and water, at the B3LYP/6-311++G(d,p) level using the PCM. The compound has a comparatively large HOMO–LUMO energy gap ($\Delta E = 5.6015$ eV) in the gas-phase, *i.e.*, high kinetic stability and low inherent chemical reactivity [21]. The HOMO energy (-6.67 eV) is an index of the ionization potential (IP) of the molecule, and the LUMO energy (-1.07 eV) is an index of the electron affinity (EA). From them, the global hardness ($\eta = 2.80$ eV), the softness ($S = 0.17853$ eV $^{-1}$), and a moderate dipole moment ($\mu = 0.8640$ D) are calculated, suitable for a relatively nonpolar electronic distribution in the gas-phase. Among solvent phases, a trend of increasingly higher chemical softness and polarity is observed with an increase in the dielectric constant (ϵ). Moving from benzene ($\epsilon = 2.3$) to water ($\epsilon = 78.35$), HOMO energy rises from -5.64 eV to -5.74 eV, while LUMO decreases from -1.90 eV to -2.03 eV. This stabilization of frontier orbitals, and especially the LUMO, promotes the molecule's ability to accept electrons (increased EA) and is a sign of increased tendency for electrophilic interactions [11]. ΔE consequently drops significantly from 5.60 eV (gas) to ~ 3.71 eV in polar solvents of high polarity, implying an increase in chemical reactivity and decreased kinetic stability [28]. Global hardness (η) also exhibits a parallel trend, decreasing from 2.80 eV in vacuum to 1.85 eV in water. As a reciprocal function, the softness (S) increases to 0.26959 eV $^{-1}$, corroborating the fact that the compound is softer and more reactive in polar solvents chemically. Soft molecules will more readily undergo charge transfer and are therefore useful for electron transport, coordination chemistry, or bio-binding applications [29]. The dipole moment (μ), a measure of the net polarity, also rises consistently across the solvent continuum,

from 0.8640 D in the gas-phase to 1.2416 D in water. This would signify strong polarization of the molecule by the solvent, which may increase its potential solubility, hydrogen bonding, and electrostatic interactions in aqueous or biological media [30].

Table 3. Calculated energies, frontier orbital energies, chemical hardness and dipole moments of structure for six different solvents.

DFT/B3LYP/6-311++G(d,p)							
	Gas-phase	Benzene	Dichloromethane	Ethanol	Methanol	DMSO	Water
	($\epsilon = 1$)	($\epsilon = 2.3$)	($\epsilon = 8.93$)	($\epsilon = 24.55$)	($\epsilon = 32.61$)	($\epsilon = 46.7$)	($\epsilon = 78.35$)
E_{total} (Hartree)	-706.9257	-706.9289	-706.9321	-706.9331	-706.9332	-706.9334	-706.9335
E_{HOMO} (eV)	-6.6698	-5.6439	-5.7090	-5.7302	-5.7334	-5.7364	-5.7394
E_{LUMO} (eV)	-1.0683	-1.8983	-1.9894	-2.0180	-2.0221	-2.0262	-2.0300
ΔE (eV)	5.6015	3.7456	3.7195	3.7122	3.7113	3.7103	3.7095
EA (eV)	1.0683	1.8983	1.9894	2.018	2.0221	2.0262	2.0300
IA (eV)	6.6698	5.6439	5.7090	5.7302	5.7334	5.7364	5.7394
η (eV)	2.8007	1.8728	1.8598	1.8561	1.8557	1.8551	1.8547
S (eV) ⁻¹	0.17853	0.26698	0.2688	0.26938	0.26944	0.26953	0.26959
μ (D)	0.8640	1.0354	1.1846	1.2250	1.2307	1.2363	1.2416

By comparing trends across the solvents, dichloromethane ($\epsilon = 8.93$), although moderately polar, already leads to a significant decrease in ΔE (3.72 eV) compared to benzene (3.75 eV), showing that even intermediate dielectric constant solvents can cause major effects on molecular orbital energies. From ethanol ($\epsilon = 24.55$) to water ($\epsilon = 78.35$), the trend weakens, suggesting that the stabilization effect asymptotically saturates in high-dielectric media. Notably, the IP steadily decreases from 6.67 eV in the gas-phase to 5.74 eV in water, suggesting a reduced energy requirement for electron removal in solvated media. On the contrary, EA increases from 1.07 eV to 2.03 eV through the same phase transition and raises the capacity of the molecule for electron density acceptability. All these transformations together result in less chemical hardness and higher softness and therefore augment the reactivity and electrophilicity of the molecule in polar solvents. These findings are of great significance in understanding solvent-dependence in reactivity, especially for drug delivery, molecular docking, or catalytic systems where the molecule would behave differently under solvated conditions versus vacuum. A case in point is the way that the higher dipole moment and electron affinity in aqueous conditions imply the molecule might form more robust electrostatic interactions or hydrogen bonding with polar surfaces or biomolecules. Thus, environmental context is critical in the prediction of I^+ 's behavior in chemical and biological systems.

3.5. Mulliken Population Analysis and Natural Population Analysis (NPA)

Fig. 4 and Table 4 show an extensive comparison of Mulliken and natural population analysis (NPA) atomic charges of the 1,3-bis(4-methylphenyl)triazene molecule computed at the B3LYP/6-311++G(d,p) level of theory and present significant discrepancies in the representation of electron density distribution of each method.

Table 4. Mulliken population method and natural population analysis computed net charges.

Atom	Mulliken Charge (e)	Natural Charge (e)	Atom	Mulliken Charge (e)	Natural Charge (e)
N1	-0.272712	-0.36401	C14	-0.454350	-0.58663
N2	0.335148	-0.01933	H1N	0.296565	0.36940
N3	-0.053903	-0.28937	H2	0.124905	0.20021
C1	-0.175407	0.14266	H3	0.153858	0.20049
C2	-0.279626	-0.22865	H5	0.189110	0.20408
C3	-0.523758	-0.18639	H6	0.152859	0.22505
C4	0.609253	-0.05291	H8	0.174485	0.21128
C5	-0.405058	-0.17695	H9	0.129688	0.19934
C6	0.058272	-0.22210	H11	0.198333	0.20217
C7	-0.448971	0.09474	H12	0.129791	0.21904
C8	-0.159797	-0.18333	H13A	0.152988	0.21043
C9	-0.654359	-0.20446	H13B	0.150309	0.20358
C10	0.621482	-0.02816	H13C	0.161224	0.21464
C11	-0.233903	-0.19161	H14A	0.138482	0.20342
C12	0.087519	-0.19921	H14B	0.142743	0.20810
C13	-0.515885	-0.58932	H14C	0.170717	0.21386

Both techniques assign small, positive partial charges to hydrogen atoms -with Mulliken charges from about +0.12 e to +0.30 e and NPA values from +0.20 e to +0.37 e- demonstrating consistency for these less electronically advanced atoms. But wide divergences arise in charging heavier atoms, which indicate methodological limitations built into Mulliken population analysis. For instance, Mulliken saddles the inner nitrogen atom N2 with an enormous positive charge of +0.335 e, whereas NPA places this atom at nearly neutral or very slightly negative (-0.019 e), which is a glaring overestimation by Mulliken due to its extreme basis set dependence and overlap of atomic orbitals. Correspondingly, Mulliken reports highly positive charges on C4 and C10 carbon atoms (around +0.609 e and +0.621 e, respectively) compared to NPA results, which report the atoms as strongly near neutral or slightly negative atoms (-0.053 e and -0.028 e, respectively), and which shows that Mulliken doesn't capture effects of electron delocalization and polarization effectively. Additional discrepancies for atoms C3 and C7 are observed such that Mulliken charges are not only of the opposite sign from the corresponding values of NPA but also varying in magnitude. Additionally, the carbon atoms from the methyl-substituted phenyl rings at positions C13 and C14 exhibit unusually significant negative charges during the NPA analysis (*ca.* -0.59 e), contrasting with less negative values in Mulliken, as highlighting NPA's enhanced management of π -electron density and conjugation. These discrepancies indicate that Mulliken population analysis, beneficial as it may be for fast and rough evaluation, tends to produce chemically unreasonable or excessively high charge distributions, especially in systems with delocalized electrons or polar bonds. In contrast, NPA gives more chemically useful and physically reasonable atomic charge descriptions because of its lesser sensitivity to the choice of basis set and due to the utilization of natural localized molecular orbitals. The overall trend is that NPA produces lower-magnitude values for charge and greater consistency with established electronegativity trends-assigning negative charges to more electronegative atoms (*e.g.*, nitrogen and some carbon atoms) and positive charges to less electronegative atoms (*e.g.*, hydrogen). Hence, for a molecule like **I**, where correct interpretation of electron distribution is the key to defining reactivity and intermolecular interactions, NPA would be the preferred method, and Mulliken analysis would be employed judiciously and only for comparative purposes or convention's sake.

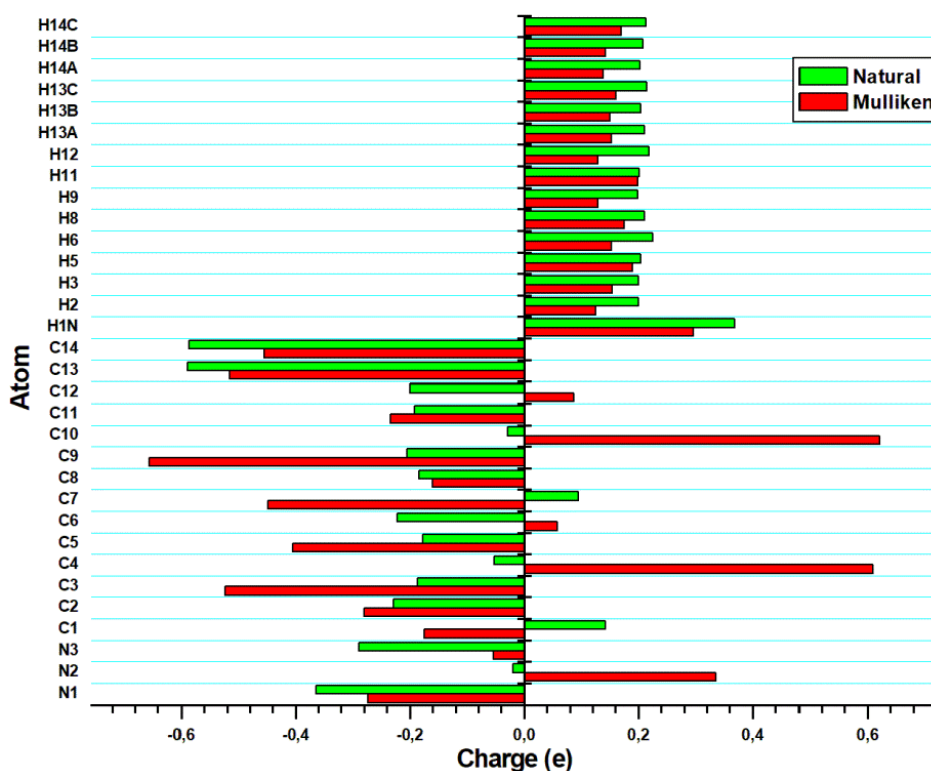


Fig. 4. Mulliken and natural charge values for the atoms of the compound graph.

3.6. Thermodynamic Properties

The thermodynamic properties as a function of temperature - constant pressure heat capacity ($C_{p,m}^0$), entropy (S_m^0), and enthalpy change (H_m^0) - for **I** were computed at the B3LYP/6-311++G(d,p) level in gas-phase from 100 to 1000 K (Table 6, Fig. 5).

These parameters provide valuable information on the thermal behavior, stability, and energy storage capacity of the molecule across a wide range of thermal conditions. The heat capacity calculated exhibits a strong, close to linear dependence on temperature with rising temperature, from 25.392 cal mol⁻¹ K⁻¹ at 100 K to 139.094 cal mol⁻¹ K⁻¹ at 1000 K. This is typical for molecular systems and is a result of the stepwise excitation of vibrational, rotational, and translational degrees of freedom with increasing thermal energy [31]. Heat capacity is dominated at low temperatures by translational and rotational modes, but at temperatures well above ~400 K, significant vibrational contributions are dominant. This monotonic increase attests to the fact

that more heat is being consumed by the molecule for each degree temperature change when it's warmer, a property useful in defining thermal buffering and stability in chemical and physical processes. The values of entropy, describing the magnitude of molecular randomness, also register a consistent increase from 91.797 cal mol⁻¹ K⁻¹ for 100 K to 259.711 cal mol⁻¹ K⁻¹ for 1000 K. The rate of rise decelerates a bit at high temperatures, showing logarithmic-like behavior characteristic of statistical thermodynamics [32]. This rise in entropy can be attributed to the increased set of available molecular microstates due to more populated vibrational and rotational motions. At 298.15 K (room temperature), the calculated entropy is 135.861 cal mol⁻¹ K⁻¹, well within the range one would anticipate for medium-sized organic molecules, again supporting the thermodynamic viability of the system. The enthalpy change at absolute zero, H⁰_m, increases significantly from 1.9463 kcal mol⁻¹ at 100 K to 87.7520 kcal mol⁻¹ at 1000 K. This growth is nearly quadratic with temperature, as it must be in the integral relationship between heat capacity and temperature [33]. H⁰_m is 10.4754 kcal mol⁻¹ under standard conditions (298.15 K), indicating that the molecule holds moderate internal energy on thermal excitation. Such behavior is an indication of growing energy content in the system and is of significance in approximating reaction enthalpies and thermal stability. In conclusion, all three thermodynamic properties - C⁰_{p,m}, S⁰_m, and H⁰_m - demonstrate smooth and physically consistent trends with temperature, validating the accuracy of the same method to model the gas-phase thermodynamic behavior of organic compounds. These findings are especially valuable for predicting reaction energetics, material design with temperature sensitivity, or further computational modeling in thermochemistry and kinetics [34].

Table 6. Temperature dependence of C⁰_{p,m}, S⁰_m and H⁰_m calculated at B3LYP/6-311++G(d,p) basis set for the molecule in gas-phase.

Temperature (K)	E (k cal mol ⁻¹)	C ⁰ _{p,m} (cal mol ⁻¹ K ⁻¹)	S ⁰ _m (cal mol ⁻¹ K ⁻¹)	H ⁰ _m (k cal mol ⁻¹)
100	165.336	25.392	91.797	1.9463
200	168.674	41.790	115.663	5.4830
298.15	173.477	59.355	135.861	10.4754
400	180.712	78.338	157.295	17.9190
500	189.351	93.948	176.950	26.7562
600	199.408	106.756	195.613	37.0122
700	210.623	117.202	213.187	48.4260
800	222.787	125.817	229.682	60.7892
900	235.739	133.015	245.163	73.9399
1000	249.353	139.094	259.711	87.7520

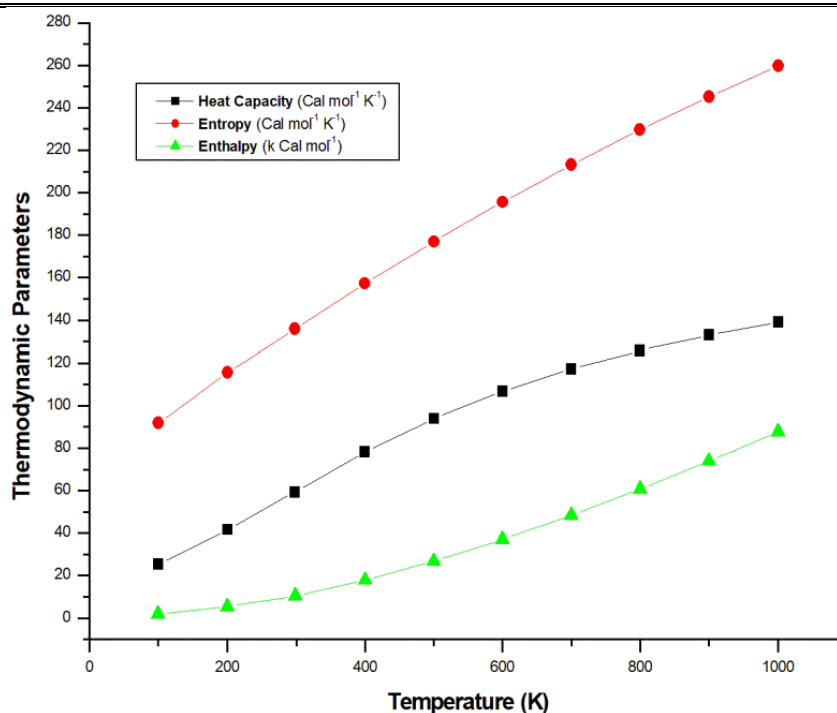


Fig. 5. Plot of calculated thermodynamic parameters vs. temperature of I in gas-phase.

To determine the temperature dependence of the thermodynamic properties of I, the computed values of the C⁰_{p,m}, S⁰_m, and H⁰_m in the gas-phase were used to fit second-order polynomial equations of the form $y = a + bT + cT^2$, where T is the temperature expressed in Kelvin. These correlations were derived from data computed from DFT calculations at the B3LYP/6-311++G(d,p) level and exhibit excellent agreement, as indicated by the high correlation coefficients (R^2). The heat capacity equation $C_{p,m}^0 = 1.49215 + 0.22799T - 9.03411 \times 10^{-5}T^2$ ($R^2 = 0.99903$) demonstrates a very strong, nearly linear rise in C⁰_{p,m} over the temperature range being studied. The positive linear term is the increasing ability of the molecule to accumulate energy with temperature, and the small negative quadratic term introduces a weak curvature, exhibiting a smooth saturation of accessible

vibrational modes at high temperatures. This is as classical and quantum statistical mechanics would predict for polyatomic molecules [31]. The entropy equation $S_m^0 = 68.3448 + 0.2432 T - 5.18755 \times 10^{-5} T^2$ ($R^2 = 0.99997$) reflects a quasi-linear rise in disorder with temperature, with minimal curvature. This is a result of the continuous thermal activation of translational, rotational, and vibrational degrees of freedom, leading to an increased number of accessible microstates. The extremely high R^2 value signals the model's strength and confirms the thermodynamic integrity of the DFT-calculated entropy values across a wide range of temperatures [32]. The enthalpy change $H_m^0 = -2.12054 + 0.02577 T + 6.49632 \times 10^{-5} T^2$ ($R^2 = 0.99952$) has a strictly increasing increase in H_m^0 with temperature, comprised of a dominant linear component and a minor accelerating quadratic component. The negative constant term is a numerical artifact of absolute zero extrapolation, with enthalpy being defined relative to the standard state. The positive coefficients for T and T^2 terms are physically meaningful, representing the accumulation of internal energy with more input of thermal energy [33]. Collectively, the good agreement between calculated data and fitted equations validate the reliability of the B3LYP/6-311++G(d,p) theory level in calculating gas-phase thermodynamics of medium-sized organic molecules. Such equations are reliable tools for predicting items based on interpolation of thermodynamic values over a continuum of temperatures and are worth employing for thermal process modeling, reaction kinetics, and materials design purposes.

3.7. Hirshfeld Surface Analysis

The d_{norm} -mapped Hirshfeld surface analysis of **I** is helpful in gaining insight into the intermolecular interactions that dictate its crystal packing. As evident from Fig. 6, close contacts are represented by deep red spots on the surface, with strong hydrogen-bonding interactions involving the nitrogen atom N3 being highlighted in particular. Two important interactions are observed: N1–H1 \cdots N3 and C2–H2 \cdots N3, both of which exhibit red spots that represent contact distances below the sum of van der Waals radii, testifying to their involvement in stabilizing the molecular assembly. Weakened interaction, C14–H14 \cdots C5, is also observed and is most probably a C–H \cdots π interaction, which is involved in the crystal structure but with lower strength, as represented by the smaller red dot. The overall red to white to blue color gradient on the Hirshfeld surface further delineates regions of strong interaction, neutral contact, and minimal interaction, respectively. All these observations point to the dominating role played by hydrogen bonding, particularly with N3, in the formation and stabilization of the compound's crystal lattice.

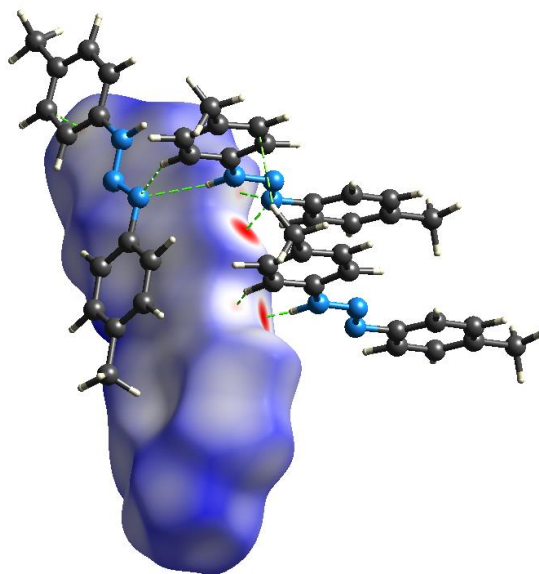


Fig. 6. The d_{norm} -mapped Hirshfeld surface for visualizing the intermolecular contacts for compound.

Fig. 7 is a precise visualization of the 3D Hirshfeld surfaces of the compound **I**, which gives a comprehensive report on its intermolecular interactions and crystal packing features. The d_{norm} -mapped surface (top left), ranging from -0.2673 to 1.4751, uses a red-white-blue color scheme to represent intermolecular contacts. Red regions, indicating negative d_{norm} values, are those contacts less than the van der Waals radii sum, e.g., N1–H1 \cdots N3 and C2–H2 \cdots N3 hydrogen bonds, bearing witness to their roles as directionality, strong interactions within the crystal lattice, also seen in Fig. 6. The d_i (inner distances) and d_e (outer distances) surfaces (upper right and center), varying from 0.9477 to 2.4926 Å and 0.9486 to 2.4218 Å, respectively, are the extent by which atoms within and outside the molecular surface are to neighboring atoms. Red and yellow areas in these maps indicate regions of tight atomic packing, while green to blue areas indicate regions of reduced interaction, indicating a heterogeneous contact environment surrounding the molecule. These mappings assist in evaluating the proximity of the molecule to its crystal neighbors from both internal and external perspectives. The shape index surface (bottom left), ranging from -1.0000 to +1.0000, is particularly well suited for the detection of π - π stacking interactions. These are indicated by the presence of alternating red (concave) and blue (convex) triangular patches on the surface of aromatic regions, suggestive of favorable overlap of π -electron systems between adjacent phenyl rings. The surface of curvedness (center bottom), from -4.0000 to 0.4000, is between flat

regions (green), typical of planar aromatic rings and potential stacking, and very curved regions (blue), associated with edges and non-planarity. These would be conducive to π - π interactions and uncover the molecular topography that is affecting crystal stability. The surface of the patch of the fragment (lower right), calculated within interval 0.0000 to 16.0000, marks chemically different regions of the molecule in various colors to give a clear indication of how different fragments of the molecule contribute to the overall interaction surface. Visualisation aids in the labelling of contact regions and topological positions of substituents and facilitates easier interpretation of structure-property relations within the lattice. Collectively, the quantitative data and visual representation of these Hirshfeld surface properties offer an extensive and well-coordinated image of the non-covalent interactions in **I**. The combination effect of intensive hydrogen bonding, π - π stacking, and van der Waals forces as described in these surface maps gives a cooperative yet complex network of interactions that controls the molecule's solid-state assembly, the crystal packing as a whole, stability, and structural coherence of the molecule.

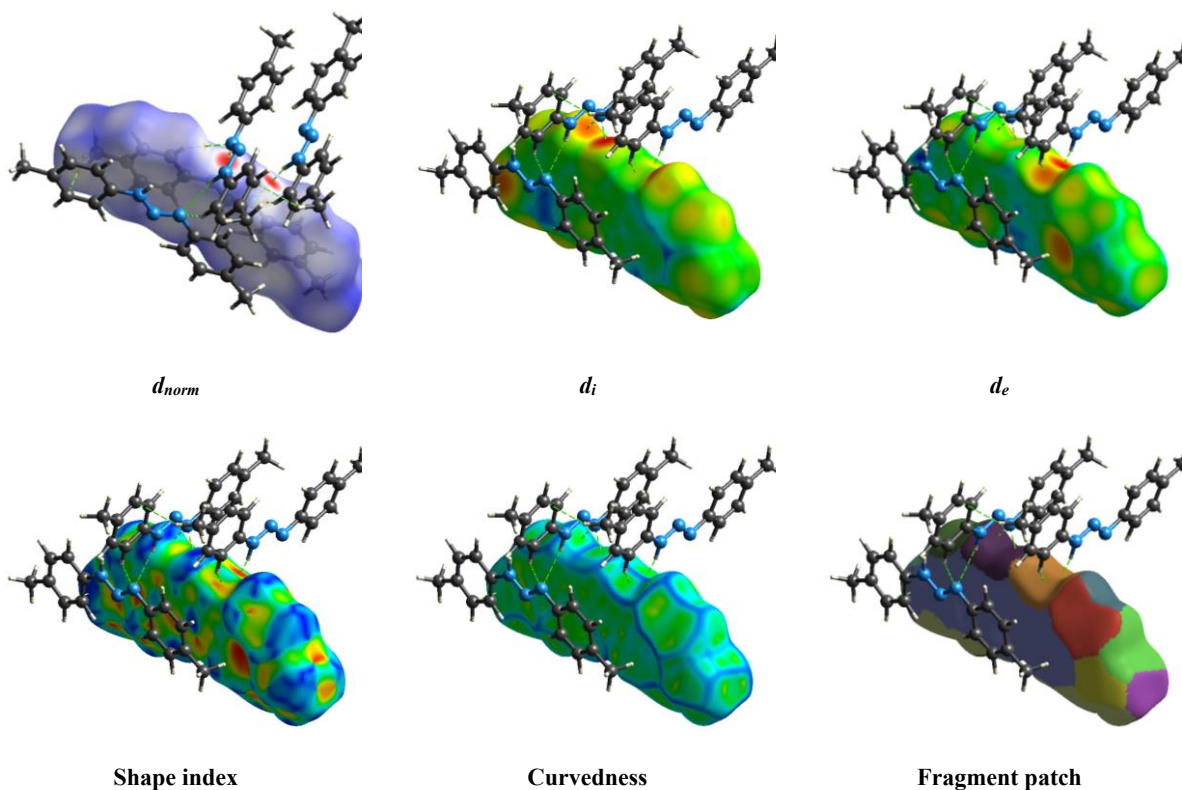


Fig. 7. View of the 3D Hirshfeld surfaces of **I**.

The Hirshfeld fingerprint of **I** shows that H \cdots H contacts are the largest ($\approx 64.5\%$ of the surface) with C \cdots H/H \cdots C ($\sim 19.6\%$) and N \cdots C/C \cdots N ($\sim 8.0\%$) being the next largest fractions (Fig. 8). Such a profile indicates a lattice stabilized mainly by weak van der Waals forces: similar studies of all-hydrogen (hydrocarbon) crystals show that very high H \cdots H fractions accompany close-packed, dispersion-bound networks [35]. Actually, though the many H \cdots H contacts neatly fill space and optimize packing efficiency, they make little directional binding energy - in fact, such contacts typically have slightly positive (repulsive) electrostatic energy [36]. By contrast, the C \cdots H/H \cdots C contacts (approximately one fifth of the total) comprise numerous C-H \cdots π and C-H \cdots N interactions, which were determined to be electrostatically attractive and “drive and control” packing in aromatic systems [36]. These weak hydrogen-bond-like contacts are often the cause of typical motifs (such as herringbone layers or ribbons) and hence supply most of the cohesive energy in this crystal. The N \cdots C/C \cdots N contacts ($\approx 8\%$) likely result from alignment of neighboring aromatic carbons with the triazene nitrogen(s) (*e.g.*, lone-pair- π or dipolar interactions), adding further (if modest) orienting stabilization. In contrast, true π - π stacking (C \cdots C contacts) virtually doesn't occur - C \cdots C contacts are next to nothing in the fingerprint - as predicted by the assumption that straightforward C-C overlaps are disfavored when C-H attractions dominate [36]. Short N \cdots H or N \cdots N contacts are also very small, indicating no important N-H hydrogen bonds or pathological H-H bonding networks. Overall, the data project an image of a tightly interwoven, tidily packed organic lattice held together by isotropic dispersion and a web of weak C-H interactions. The implication is that crystal packing is highly dense, but since there are no strong directional bonds (like conventional H-bonds or π -stacks) in operation, thermal and mechanical stability will be only moderate: melting or slipping should be quite easy to induce even with high packing density. Finally, the largely van der Waals nature and planar diaryl-triazene framework suggest potential in organic and materials chemistry applications: *e.g.*, diaryltriazene derivatives were found to function as useful reagents or intermediates in organic synthesis and have been explored as pharmaceutical (anticancer, antimicrobial) or sensing molecules [1]. Overall, the fingerprinting calls attention to a crystal stabilized by strong dispersion and moderate C-H bonding, thus enabling effective packing without implying high intrinsic stability - a set of features that is in harmony with the familiar chemically versatile properties of diaryltriazene species [35].

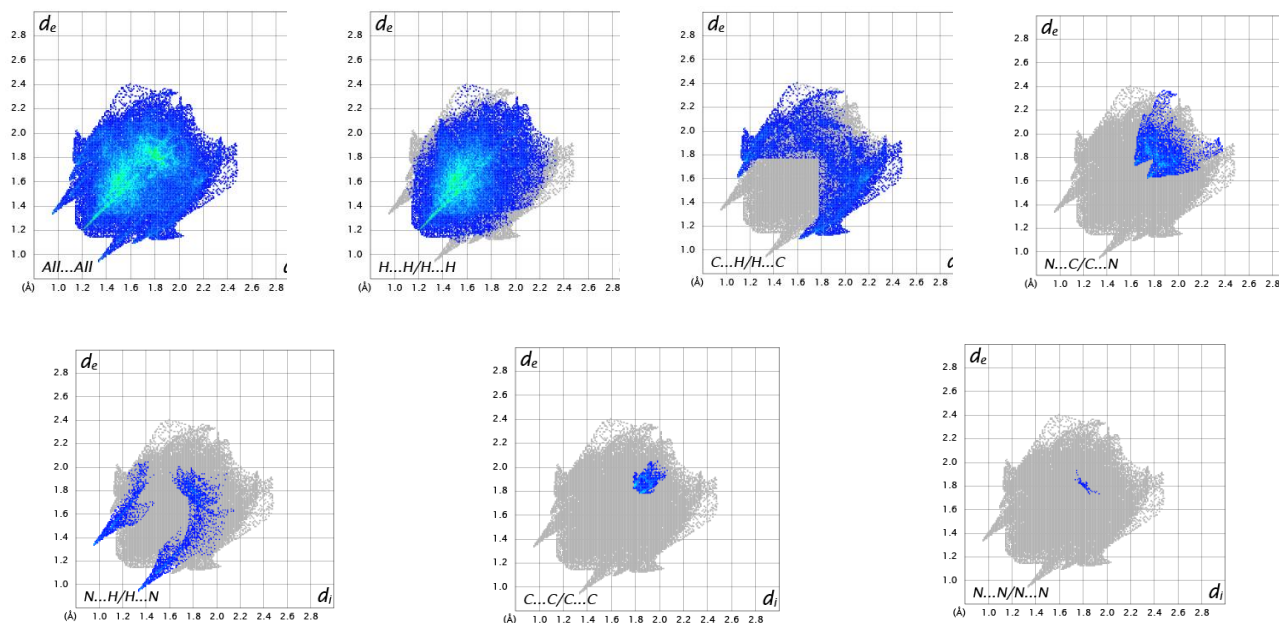


Fig. 8. All interactions of two-dimensional fingerprint plots for I.

3.8. Molecular Docking

Molecular docking simulations were carried out to examine the interaction profile of compound **I** with the human epidermal growth factor receptor 2 (HER2), a tyrosine kinase involved in mediating cell proliferation and survival signaling pathways. HER2 overexpression is known to be an instigating factor for tumorigenesis, particularly in breast and gastric cancer, and thus remains a high-priority target for anticancer therapy [17]. The docking result, computed using AutoDock Vina, was -9.8 k cal mol⁻¹ of binding energy, which is an indication of strong and thermodynamically favorable interaction comparable to the expected interaction for known HER2 inhibitors such as lapatinib and neratinib [18]. The docking experiment, as shown in Table 7 and Fig. 9, indicates that compound **I** fits well into the ATP-binding cleft of the HER2 kinase domain.

Table 7. Data from the binding simulation of the molecule against the HER2 receptor.

	Binding affinity (k cal mol ⁻¹)	Hydrophobic Interactions	Hydrogen Bond
Compound I	-9.8	Ala571	Asp803
		Lys753	Ser783
		Val734	

Hydrophobic contacts were observed between the molecule and important non-polar residues Ala571, Lys753, and Val734. The contacts are between the hydrophobic regions of the ligand and the participating amino acid side chains, primarily through van der Waals contacts and dispersion interactions. Even though Lys753 is usually a polar, basic residue, the microenvironment and alkyl side chain may both promote hydrophobic or π -cation contacts with the aryl rings of compound **I**, once more stabilizing the ligand-receptor complex [37]. In addition to such nonpolar interactions, two other important hydrogen bonds were discovered: one to Asp803, a critical catalytic residue, and the other to Ser783, which usually becomes engaged in kinase inhibitor stabilization. The hydrogen bonding to Asp803 likely stabilizes the ligand by strong electrostatic complementarity, while the binding to Ser783, as assisted by its hydroxyl group, might be linked with bifurcated hydrogen bonding to electronegative atoms on the phenyl or triazene groups. They are particularly important as they increase the binding specificity, decrease the overall binding energy, and contribute meaningfully to a more stable protein-ligand complex structure [38-41]. The triazene moiety, with its electron-rich and biologically active nature [42], is of interest in molecular recognition and electronic interactions, while the methyl-substituted aromatic rings enhance hydrophobic contact as well as lipophilicity, with a possible improvement of membrane permeability and bioavailability. Overall, these findings suggest that compound **I** is a good candidate as a lead scaffold for the construction of HER2-targeted anticancer agents. Its favourable binding energy, hydrophobic-polar interplay pair and structural components favorably lend to therapeutically active pharmacophores of kinase inhibitors and its triazene ring topology accommodates further improvement by way of functionalization or bioisosteres [43]. Although the docking results primarily focus on the studied compound, a comparison with the native ligand of the HER2 receptor (2-{2-[4-({5-chloro-6-[3-(trifluoromethyl)phenoxy]pyridin-3-yl}]amino)-5H-pyrrolo[3,2-d]pyrimidin-5-yl]ethoxy} ethanol) and structurally related analogues would indeed provide further insight into its bioactivity potential. Due to limitations in available

structural data or scope, such a comparison was not performed in detail in the current study but is considered a valuable direction for future work.

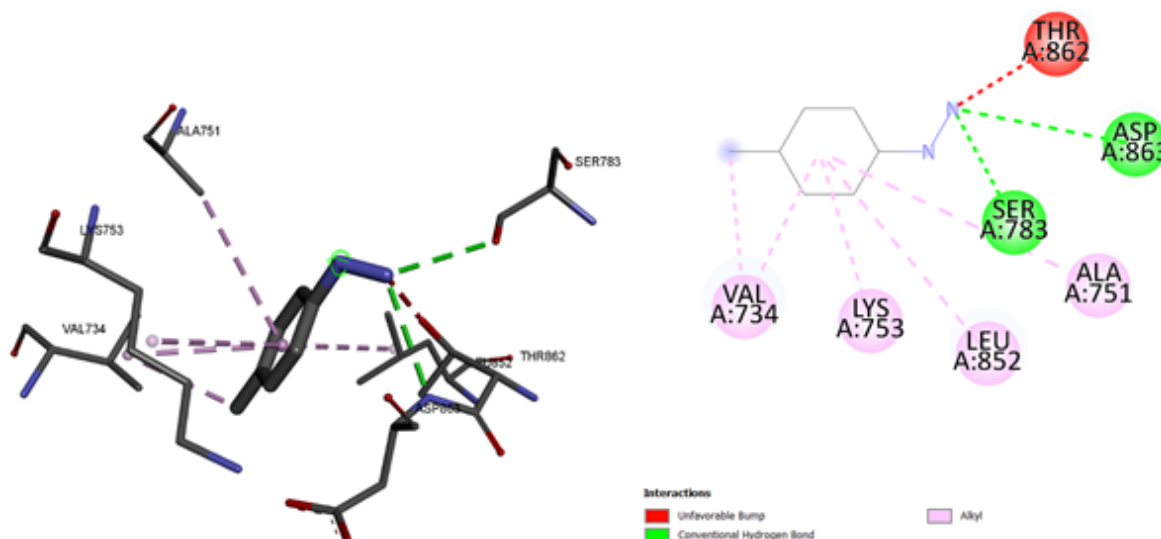


Fig. 9. Visualization of results of the HER2 receptor binding simulation with the molecule.

4. Conclusions

This study presents a comprehensive computational and structural analysis of 1,3-bis(4-methylphenyl)triazene, a diaryltriazene compound with promising pharmacological and material applications. Using density functional theory (DFT), molecular electrostatic potential (MEP), global reactivity descriptors, thermodynamic analysis, Hirshfeld surface mapping, and molecular docking, we investigated the molecule's structure, electronic properties, and biological potential. Geometry optimization at the B3LYP/6-311++G(d,p) level showed excellent agreement with crystallographic data (RMSD = 0.106 Å), confirming the reliability of DFT for modeling rigid, π -conjugated systems. The compound exhibited strong nonlinear optical (NLO) properties, with a first-order hyperpolarizability (β_{total}) nearly seven times that of urea, indicating its potential for applications in photonics and electro-optics. Frontier molecular orbital (FMO) analysis revealed a moderate HOMO–LUMO gap ($\Delta E = 5.60$ eV), suggesting a balance between reactivity and stability. In polar solvents, this gap decreased significantly (to ~ 3.71 eV in water), reflecting enhanced reactivity. Global reactivity descriptors further indicated increased electrophilicity and polarizability in such media. MEP and charge distribution analyses identified reactive sites around hydrogen and triazene nitrogen atoms, consistent with hydrogen bonding and electrostatic interactions. Thermodynamic parameters (entropy, enthalpy, heat capacity) displayed physically meaningful temperature trends, supporting the thermal stability of the model. Hirshfeld surface and fingerprint analyses showed that crystal packing is mainly stabilized by van der Waals forces and weak C–H \cdots N or C–H $\cdots\pi$ interactions, typical for diaryltriazenes. Molecular docking with the HER2 receptor (PDB ID: 3PP0) yielded a favorable binding energy (-9.8 kcal mol $^{-1}$), with key interactions involving hydrogen bonds (Asp803, Ser783) and hydrophobic contacts (Ala571, Lys753, Val734). These findings suggest potential for HER2-targeted drug development. In summary, the combined theoretical and structural results highlight the compound's dual potential in biomedical and materials science, with strong NLO response, adaptable electronic features, and promising bioactivity. Future experimental studies are encouraged to validate its application in therapeutic and optoelectronic domains.

References

- [1] P. de M. S. Figueirêdo *et al.*, “Assessment of the biological potential of diaryltriazene-derived triazene compounds,” *Sci. Rep.*, vol. 11, p. 2541, 2021.
- [2] F. Marchesi, M. Turriziani, G. Tortorelli, G. Avvisati, F. Torino, ve L. De Vecchis, “Triazene compounds: Mechanism of action and related DNA repair systems,” *Pharmacol. Res.*, vol. 56, no. 4, pp. 275-287, 2007.
- [3] N. Iqbal ve N. Iqbal, “Human epidermal growth factor receptor 2 (HER2) in cancers: Overexpression and therapeutic implications,” *Mol. Biol. Int.*, vol. 2014, p. 852748, 2014.
- [4] S. Lamichhane, R. P. Rai, A. Khatri, R. Adhikari, B. G. Shrestha, ve S. K. Shrestha, “Screening of phytochemicals as potential anti-breast cancer agents targeting HER2: An in-silico approach,” *J. Biomol. Struct. Dyn.*, vol. 41, no. 3, pp. 897-911, 2023.
- [5] R. B. O. Ouma, S. M. Ngari, ve J. K. Kibet, “A review of the current trends in computational approaches in drug design and metabolism,” *Discov. Public Health*, vol. 21, p. 108, 2024.

- [6] P. C. Agu *et al.*, "Molecular docking as a tool for the discovery of molecular targets of nutraceuticals in diseases management," *Sci. Rep.*, vol. 13, no. 1, p. 13398, 2023. doi: 10.1038/s41598-023-40160-2
- [7] M. J. Frisch *et al.*, *Gaussian 03, Revision C.02*, Gaussian, Inc., 2004.
- [8] C. Lee, W. Yang, ve R. G. Parr, "Development of the Colle-Salvetti correlation-energy formula into a functional of the electron density," *Phys. Rev. B*, vol. 37, no. 2, pp. 785-789, 1988. doi: 10.1103/PhysRevB.37.785
- [9] A. D. Becke, "Density-functional thermochemistry. III. The role of exact exchange," *J. Chem. Phys.*, vol. 98, no. 7, pp. 5648-5652, 1993. doi: 10.1063/1.464913
- [10] R. Dennington, T. Keith, ve J. Millam, *GaussView, Version 5.0* [Computer software], Semichem Inc., 2009.
- [11] R. G. Parr, L. V. Szentpály, ve S. Liu, "Electrophilicity index," *J. Am. Chem. Soc.*, vol. 121, no. 9, pp. 1922-1924, 1999. doi: 10.1021/ja983494x
- [12] J. Tomasi, B. Mennucci, ve R. Cammi, "Quantum mechanical continuum solvation models," *Chem. Rev.*, vol. 105, no. 8, pp. 2999-3094, 2005. doi: 10.1021/cr9904009
- [13] M. J. Turner *et al.*, *CrystalExplorer17* (Version 17.5) [Computer software], University of Western Australia, 2017.
- [14] J. J. McKinnon, D. Jayatilaka, ve M. A. Spackman, "Towards quantitative analysis of intermolecular interactions with Hirshfeld surfaces," *Chem. Commun.*, no. 37, pp. 3814-3816, 2007. doi: 10.1039/B704980C
- [15] M. A. Spackman ve D. Jayatilaka, "Hirshfeld surface analysis," *CrystEngComm*, vol. 11, no. 1, pp. 19-32, 2009. doi: 10.1039/B818330A
- [16] F. L. Hirshfeld, "Bonded-atom fragments for describing molecular charge densities," *Theor. Chim. Acta*, vol. 44, no. 2, pp. 129-138, 1977. doi: 10.1007/BF00549096
- [17] K. Aertgeerts *et al.*, "Structural analysis of the mechanism of inhibition and allosteric activation of the kinase domain of HER2 protein," *J. Biol. Chem.*, vol. 286, no. 21, pp. 18756-18765, 2011. doi: 10.1074/jbc.M110.206193
- [18] O. Trott ve A. J. Olson, "AutoDock Vina: improving the speed and accuracy of docking with a new scoring function, efficient optimization and multithreading," *J. Comput. Chem.*, vol. 31, no. 2, pp. 455-461, 2010.
- [19] D. Biovia *et al.*, *Discovery Studio Visualizer* (Version 17.2) [Computer software], Dassault Systèmes, 2016.
- [20] N. Karadayı, Ş. Çakmak, M. Odabaşoğlu, ve O. Büyükgüngör, "1,3-Bis(4-methylphenyl)triazene, 1-(4-chlorophenyl)-3-(4-fluorophenyl)triazene and 1-(4-fluorophenyl)-3-(4-methylphenyl)triazene," *Acta Crystallogr. Sect. E Struct. Rep. Online*, vol. 61, no. 5, pp. o303-o305, 2005. doi: 10.1107/S0108270105004373
- [21] R. G. Parr ve W. Yang, *Density-functional theory of atoms and molecules*. Oxford University Press, 1989.
- [22] W. Koch ve M. C. Holthausen, *A chemist's guide to density functional theory*, 2nd ed. Wiley-VCH, 2001.
- [23] Y. Zhao ve D. G. Truhlar, "Density functional theory for highly excited states: The role of exact exchange," *J. Chem. Phys.*, vol. 128, no. 18, p. 184103, 2008. doi: 10.1063/1.2928720
- [24] Y. Zhao, Y. Xie, ve H. F. Schaefer, "Benchmark studies of dipole moments and first hyperpolarizabilities of push-pull π -conjugated systems," *Theor. Chem. Acc.*, vol. 116, no. 1, pp. 131-137, 2006. doi: 10.1007/s00214-005-0023-6
- [25] W. Kohn ve L. J. Sham, "Self-consistent equations including exchange and correlation effects," *Phys. Rev.*, vol. 140, no. 4A, pp. A1133-A1138, 1965. doi: 10.1103/PhysRev.140.A1133
- [26] P. Politzer ve J. S. Murray, "The fundamental nature and role of the electrostatic potential in atoms and molecules," *Theor. Chem. Acc.*, vol. 108, no. 3, pp. 134-142, 2002. doi: 10.1007/s00214-002-0363-9
- [27] W. Yang ve R. G. Parr, "Hardness, softness, and the Fukui function in the electronic theory of metals and catalysis," *Proc. Natl. Acad. Sci. U.S.A.*, vol. 82, no. 20, pp. 6723-6726, 1985. doi: 10.1073/pnas.82.20.6723
- [28] P. Geerlings, F. De Proft, ve W. Langenaeker, "Conceptual density functional theory," *Chem. Rev.*, vol. 103, no. 5, pp. 1793-1874, 2003. doi: 10.1021/cr990029p
- [29] R. G. Parr ve R. G. Pearson, "Absolute hardness: companion parameter to absolute electronegativity," *J. Am. Chem. Soc.*, vol. 105, no. 26, pp. 7512-7516, 1983. doi: 10.1021/ja00364a005
- [30] C. J. Cramer ve D. G. Truhlar, "Implicit solvation models: Equilibria, structure, spectra, and dynamics," *Chem. Rev.*, vol. 99, no. 8, pp. 2161-2200, 1999. doi: 10.1021/cr960149m
- [31] D. A. McQuarrie ve J. D. Simon, *Physical chemistry: A molecular approach*. University Science Books, 1999.
- [32] P. Atkins ve J. de Paula, *Atkins' physical chemistry*, 10th ed. Oxford University Press, 2014.
- [33] K. S. Pitzer, E. R. Lippincott ve R. F. Curl, "The Thermodynamic Properties of Organic Compounds," *J. Am. Chem. Soc.*, vol. 67, no. 8, pp. 1341-1350, 1945. doi: 10.1021/ja01224a002
- [34] L. A. Curtiss, K. Raghavachari, P. C. Redfern ve J. A. Pople, "Assessment of Gaussian-2 and density functional theories for the computation of enthalpies of formation," *J. Chem. Phys.*, vol. 106, no. 3, pp. 1063-1079, 1997. doi: 10.1063/1.473182
- [35] A. N. Khalilov *et al.*, "Crystal structure and Hirshfeld surface analysis of (2E)-1-phenyl-3-(4-fluorophenyl)prop-2-en-1-one," *Acta Crystallogr. Sect. E: Crystallogr. Commun.*, vol. 78, no. 2, pp. 525-529, 2022. doi: 10.1107/S2056989022000343
- [36] C. Jelsch ve Y. B. M. Bisseyoub, "Deciphering the driving forces in crystal packing by analysis of intermolecular interactions in aromatic hydrocarbons," *IUCrJ*, vol. 10, no. 5, pp. 557-567, 2023. doi: 10.1107/S2056989023005043
- [37] C. Bissantz, B. Kuhn ve M. Stahl, "A medicinal chemist's guide to molecular interactions," *J. Med. Chem.*, vol. 53, no. 14, pp. 5061-5084, 2010. doi: 10.1021/jm100112j
- [38] S. Başak ve C. C. Ersanlı, "Structure elucidation of Schiff base-containing compound by quantum chemical methods," *Int. Sci. Vocat. Stud. J.*, vol. 8, no. 2, pp. 129-136, 2024. doi: 10.47897/bilmes.1553500

- [39] C. C. Ersanlı ve S. Başak, "Quantum Mechanical Calculations and Molecular Docking Simulation Studies of *N*-(5-chloro-2-oxobenzyl)-2-hydroxy-5-methylanilinium Compound," *Int. Sci. Vocat. Stud. J.*, vol. 8, no. 2, pp. 162-177, 2024. doi: 10.47897/bilmes.1573560
- [40] S. Öztürk, T. Aycan, Z. Demircioğlu ve C. C. Ersanlı, "Quantum Mechanical Calculations, Hirshfeld Surface Analysis, Molecular Docking, ADME and Toxicology Studies of the Ethyl 4-chloro-2-[(4-nitrophenyl)hydrazono]-3-oxobutrate Compound," *Int. Sci. Vocat. Stud. J.*, vol. 7, no. 2, pp. 109-121, 2023. doi: 10.47897/bilmes.1385170
- [41] D. B. Kitchen, H. Decornez, J. R. Furr ve J. Bajorath, "Docking and scoring in virtual screening for drug discovery: methods and applications," *Nat. Rev. Drug Discov.*, vol. 3, no. 11, pp. 935-949, 2004. doi: 10.1038/nrd1549
- [42] D. E. V. Wilman, "Triazines as antitumor agents," *Med. Res. Rev.*, vol. 8, no. 1, pp. 1-20, 1988. doi: 10.1002/med.2610080102
- [43] C. N. Cavasotto ve A. J. W. Orry, "Ligand docking and structure-based virtual screening in drug discovery," *Curr. Top. Med. Chem.*, vol. 7, no. 10, pp. 1006-1014, 2007. doi: 10.2174/156802607780906468